Hydrodynamic Dimensions, Electrophoretic Mobility, and Stability of Hydrophilic Quantum Dots

Thomas Pons,[†,§] **H. Tetsuo Uyeda,**[†,||] **Igor L. Medintz,**[‡] **and Hedi Mattoussi*,**[†]

Optical Sciences Division and Center for Bio/Molecular Science and Engineering, Naval Research Laboratory, Washington, DC, 20375, and Chemical and Biomolecular Engineering Department, Johns Hopkins University, Baltimore, Maryland 21218

Received: August 4, 2006

Luminescent semiconductor quantum dots (QDs) have great potential for use in biological assays and imaging. These nanocrystals are capped with surface ligands (bifunctional molecules, amphiphilic polymers, phospholipids, etc.) that render them hydrophilic and provide them with functional properties. These coatings alters their hydrodynamic radii and surface charge, which can drastically affect properties such as diffusion within the cell cytoplasm. Heavy atom techniques such as transmission electron microscopy and X-ray scattering probe the inorganic core and do not take into account the ligand coating. Herein we use dynamic light scattering to characterize the hydrodynamic radius (R_H) of CdSe–ZnS QDs capped with various hydrophilic surface coatings (including dihydrolipoic acid and amphiphilic polymers) and self-assembled QD–protein bioconjugates. Experiments were complemented with measurements of the geometric size and zeta potential using agarose gel electrophoresis and laser Doppler velocimetry. We find that the effects of surface ligands on the hydrodynamic radius and on the nanoparticle mobility are complex and strongly depend on a combination of the inorganic core size and nature and lateral extension of the hydrophilic surface coating. These properties are critical for the design of QD-based biosensing assays as well as QD bioconjugate diffusion in live cells.

Introduction

Semiconductor nanocrystals, or quantum dots (QDs), possess unique intrinsic optical properties that make them valuable candidates as photoluminescent probes for biological sensing and imaging.[1–6] Recent progress in developing functional, biocompatible QDs has allowed demonstration of their use in several applications, including immunoassays, single-molecule tracking, and live cell and tissue imaging.[7–14]

Reproducible synthetic routes have been developed for making QDs with high quantum yield and narrow size distribution.[15–18] However, the resulting QDs are capped with organic coatings made of primarily tri-octyl-phosphine/tri-octyl-phosphine oxide (TOP/TOPO) ligands and are only soluble in organic solvents. Use of QDs in a biological environment thus requires that they are made hydrophilic. Several water solubilization strategies have been developed. One approach involves replacing the initial TOP/TOPO cap with bifunctional ligands capable of binding the QD surface, typically via thiol–metal interaction, and possessing hydrophilic end groups. Examples of ligands include mercapto-acetic acid (MAA),[2] dihydrolipoic acid (DHLA), and poly(ethylene glycol)-terminated dihydrolipoic acid (DHLA-PEG) ligands.[3,19] Another approach involves encapsulating the organic (TOP/TOPO-coated) QDs within amphiphilic polymer shells[20,21] or lipid micelles.[7] The hydrophobic carbon chains of these molecules interdigitate with the TOP/TOPO ligands while the hydrophilic block provides water solubility. In both cases, hydrophilicity is obtained by charged groups (carboxylic acids, amines, etc.) and/or poly(ethylene glycol) (PEG) polymers. These ligands create a solubilization layer and strongly influence the hydrodynamic size of QDs along with their surface charge and mobility.

Little is known about the charge and hydrodynamic radius of water-soluble QDs or QD bioconjugates, even though these parameters are crucial, since they influence properties such as assay design, delivery, and migration of both QDs and QD bioconjugates in live cells and tissues. As a consequence, systematic characterization of the QD hydrodynamic size and surface charge are needed to control and optimize QD ligand chemistry, bioconjugation, and performance in biological assays or imaging.

While the geometric size of the inorganic core has been extensively characterized using techniques such as transmission electron microscopy (TEM) and X-ray scattering,[15,18,22] these techniques do not provide any information on the QD hydrodynamic size, which is a more relevant parameter in a biological environment. Atomic force microscopy (AFM) is sensitive to the ligand shell but requires surface immobilization and only surveys a few particles at the same time. Fluorescence correlation spectroscopy has been successfully used to characterize QD properties[23,24] but is potentially complicated by photophysical parameters, such as saturation intensity, bleaching, and the blinking dynamics present at all time scales.[25] These limitations are circumvented by dynamic light scattering (DLS), which gives direct access to the nanoparticle hydrodynamic size and polydispersity index. It only relies on the analysis of scattered light and is therefore insensitive to the influence of photophysical parameters; it is equally suited for the characterization of

* Author to whom correspondence should be addressed. E-mail: hedimat@ccs.nrl.navy.mil.
† Optical Sciences Division, Naval Research Laboratory.
‡ Center for Bio/Molecular Science and Engineering, Naval Research Laboratory.
§ Chemical and Biomolecular Engineering Department, Johns Hopkins University.
|| Present address: Promega Biosciences, Inc., 277 Granada Dr., San Luis Obispo, CA 93401.

Properties of Hydrophilic Quantum Dots

J. Phys. Chem. B, Vol. 110, No. 41, 2006 **20309**

TABLE 1: Structure and Molecular Weights (M_w) of the Ligands Used in This Work

name	structure	M_w (g/mol)
TOPO		386.65
DHLA		208.34
DHLA-PEG600 (n~12)		781.02
DHLA-PEG1000 (n~21)		1,133.44
MUA		218.36
DPPE-PEG2000		2,749.43

nonfluorescent nanoparticles (e.g., magnetic particles). Furthermore, the advent of avalanche photodiode (APD) detection and sophisticated photon correlation systems allow analysis of nanometer size particles that provide weaker scattering signals than larger colloid particles (such as polystyrene beads).

In this work, we characterize and compare the hydrodynamic size of TOP/TOPO, DHLA, and DHLA-PEG polymer-coated and lipid-micelle-encapsulated CdSe−ZnS QDs. We also use agarose gel electrophoresis (AGE) with Ferguson analysis and laser Doppler velocimetry (LDV) to provide an independent determination of QD and QD bioconjugate sizes, zeta potentials, and electrophoretic mobilities in solution.

Materials and Methods

CdSe QDs, CdSe−ZnS Core−Shell QDs and Ligands. CdSe QDs were synthesized using a high-temperature solution reaction of organometallic precursors (namely, dimethyl cadmium or cadmium 2,4-pentanedionate and TOPO:Se) in hot coordinating solvent mixtures made primarily of TOP/TOPO mixed with hexadecylamine (HDA), 1,2-hexadecanediol (HDDO), and phosphonic acids.[15,16,26] The CdSe nanocrystals were overcoated with a thin layer of ZnS using similar reaction schemes from Zn and sulfur precursors to provide CdSe−ZnS core−shell QDs.[17,18] As prepared, both CdSe and CdSe−ZnS QDs are primarily capped with TOP/TOPO mixed with a small fraction of amine ligands; they will be referred to as TOP/TOPO-capped QDs. CdSe and CdSe−ZnS were spectroscopically characterized by the location of their first absorption peak and/or fluorescence maximum.[15] CdSe core geometric sizes were estimated using published results (TEM in particular).[22,27]

DHLA and DHLA-PEG ligands (Table 1) were synthesized and used for cap exchange following our previously published procedures.[3,19] Mercaptoundecanoic acid (MUA)-capped QDs were prepared from TOP/TOPO-capped nanocrystals using commercial ligands (Sigma-Aldrich, St. Louis, MO) and following the same method used for DHLA and dispersed in water with potassium *tert*-butoxide (final pH ∼9). Light scattering and gel electrophoretic data were collected from samples shortly after preparation and after 2, 4, 6, and 8 days of storage. Cap exchange of TOP/TOPO with DHLA and DHLA-PEG ligands was verified using ^{1}H NMR and probing changes in the thiol resonances of the free ligand, before and after cap exchange and removal of excess unreacted ligand.[19] Figure 1 shows that the doublet and triplet splitting pattern for the two disparate

thiol resonances at 1.2−1.3 ppm, characteristic of the reduced dithiol moiety in the spectrum of DHLA alone, are not present in the one collected from DHLA-capped nanocrystals. Furthermore, the NMR signals due to TOP/TOPO ligands at 1.2 and 3.7 ppm in the spectrum collected from a solution of TOP/TOPO-capped QDs are essentially nonexistent in the sample of DHLA-capped nanocrystals. The other peaks at 1.4−1.6, 2.25 and 2.6, and 2.8 ppm (characteristic of the rest of the DHLA ligand) stayed intact after cap exchange, except for a small shift attributed to a change in its environment. This clearly indicates that cap exchange from TOP/TOPO to DHLA is highly efficient and that the dithiol affinity to the surface drives binding to the QDs, not the carboxylic acid end groups.

Lipid-micelle-encapsulated QDs were prepared using 1,2-dipalmitoyl-*sn*-glycero-3-phosphoethanolamine-*N*-[methoxy-(poly(ethylene glycol))-2000] (DPPE-PEG2000) (Avanti Polar Lipids, Alabaster, AL) using literature methods.[7] Carboxylic-acid-modified polymer-coated 565-nm-emitting QDs (565-nm-COOH-Qdot, catalog no. 2133-1) were purchased from Quantum Dot Corporation (Hayward, CA). Carboxylic-acid-modified T1 ("polymer coating") and T2 ("natural coating") 560-nm-emitting QDs (560-nm-COOH-T1/T2-Evident) were purchased from Evident Technologies (Troy, NY). Maltose binding proteins were engineered to have a C-terminal penta-histidine tail (MBP−His5) using procedures described in ref 28. The polyhistidine tract allows protein self-assembly on DHLA-capped QDs via metal-affinity interactions.[29]
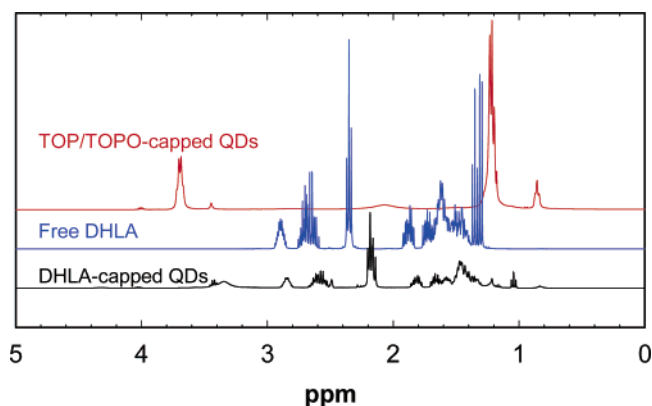
Figure 1. ^{1}H NMR spectra of TOP/TOPO, DHLA, and DHLA-capped CdSe−ZnS QDs highlighting the QD cap exchange of TOP/TOPO with DHLA.

Dynamic Light Scattering: Background. Dynamic or quasi-elastic light scattering, DLS or QELS, relies on the detection and analysis of the interference of electric fields scattered by inhomogeneities in a medium subject to an electromagnetic irradiation. The amplitude of the scattered signal strongly depends on the characteristic sizes of these inhomogeneities. In solutions where inhomogeneities are caused by dispersed objects such as polymers or colloidal nanoparticles, the amplitude of the scattered signal varies as the sixth power of their size. Furthermore, Brownian motion of these diffusing particles gives rise to concentration fluctuations and scattered signals that are time-dependent. Analysis of the time-dependent scattered intensity provides a measure of the particle diffusion coefficient and hydrodynamic size and information about the presence of aggregates.[30,31]

Experimentally, one measures the normalized autocorrelation function of the scattered intensity $I_S(t)$ at an angle θ with respect to the direction of the incident beam (homodyne light scattering) expressed as

$$G^{(2)}(\tau) = \frac{\langle I_S(t) I_S(t+\tau) \rangle_t}{\langle I_S(t) \rangle_t^2} \tag{1}$$

where $\langle \cdots \rangle_t$ denotes an average over time. This is directly related to the electric field autocorrelation function, $g^{(1)}(\tau) = a|G^{(2)}(\tau) - 1|^{1/2}$, where the constant a is proportional to the amplitude of the scattered signal. For solutions of monodisperse colloidal nanoparticles, polymers, proteins, etc. in the dilute regime (isolated objects), $g^{(1)}(\tau)$ follows a monoexponential decay with time

$$g^{(1)}(\tau) = a \exp(-\Gamma\tau) \tag{2}$$

The decay rate Γ depends on the scattering wavevector q (via θ) and the particle diffusion coefficient D

$$\Gamma = Dq^2 \quad \text{and} \quad q = \frac{4\pi n}{\lambda} \sin\left(\frac{\theta}{2}\right) \tag{3}$$

where n and λ designate the refractive index of the medium and the wavelength of the incident radiation, respectively.

It is, however, known that dispersed materials are always subject to inhomogeneous distribution in size and/or molecular weight, which translates to a departure of the correlation function from the ideal monoexponential form (eq 2). Size distribution can be described using, for example, Gaussian or log-normal distribution functions.[30] The cumulant analysis is commonly used to account for effects of size and molecular weight inhomogeneities by expressing the correlation function as[30,32]

$$g^{(1)}(\tau) = a \exp\left(-\Gamma\tau + \frac{\mu_2}{2}\tau^2 + \cdots\right) \tag{4}$$

where the first cumulant is the decay rate Γ. The second cumulant μ_2 provides information about the polydispersity index (PDI) of the measurement

$$\text{PDI} \equiv \left(\frac{\text{size distribution width}}{\text{mean size}}\right)^2 = \frac{\mu_2}{\Gamma^2} \tag{5}$$

In practice the decay rate Γ is extracted by measuring the autocorrelation function at several angles θ for each sample. Plotting Γ versus q^2 yields a linear curve, the slope of which provides an estimate for the effective diffusion coefficient (eq 3). At larger angles data may depart from linear behavior (due

to interparticle interference since smaller length scales are probed), and D is extracted from the slope at $q = 0$.

Interparticle interactions affect the measured diffusion coefficient, and an apparent concentration-dependent diffusion coefficient is thus measured. In the dilute regime where interactions are small, the effective diffusion coefficient has a linear dependence on concentration c[30]

$$D_T = D_0(1 + k_d c) \tag{6}$$

where the sign of k_d reflects the type of interparticle interactions and D_0 corresponds to the diffusion of single particles; it is extracted from extrapolation at $c = 0$. For all our samples $k_d > 0$ (though small), which corresponds to repulsive interactions (see below). This interparticle repulsion is necessary for dispersion stability. Finally, assuming that particles are spherical, the hydrodynamic radius R_H is obtained from the Stokes−Einstein relation

$$R_H = \frac{kT}{6\pi\eta_s D_0} \tag{7}$$

where η_s is the solution viscosity.

If multiple populations of scattering particles are present in the medium, such as aggregates along with monoparticles, then the scattered signal will be strongly weighted toward larger-size populations, due to the strong size dependence of the scattered intensity ($\propto R^6$); these will dominate contributions at small q. A simple cumulants analysis will provide erroneous results. To better account for the presence of aggregates and eventually delineate their contributions, the scattered intensity can be treated as a superposition of the contribution from each population i (having a characteristic size R_i)

$$g_\Sigma^{(1)}(\tau) \approx \Sigma\, a_i \exp(-\Gamma_i\tau) \tag{8}$$

where the terms a_i and Γ_i depend on R_i. A further refined analysis of scattered data from such samples uses the inverse Laplace transform, which implies writing the above expression in a more continuous form using

$$g_\Sigma^{(1)}(\tau) = \int G(\Gamma) \exp(-\Gamma\tau)\, d\Gamma \tag{9}$$

The Laplace function $G(\Gamma)$ would provide discrete peaks centered at Γ_i, each of which corresponds to the decay rate (and diffusion coefficient) of a population i.

For our measurements we used a CGS-3 goniometer system equipped with a HeNe laser illumination at 633 nm and a single-photon-counting avalanche photodiode for signal detection (Malvern Instruments, Southborough, MA). The autocorrelation function was performed by a ALV-5000/EPP photon correlator (ALV, Langen, Germany) and analyzed using Dispersion Technology Software (DTS) (Malvern Instruments). All QD solutions were filtered through 0.1 or 0.02 μm syringe filters (Whatman, Middlesex, U. K.). Sample temperature was maintained at 25 °C. For each sample, the autocorrelation function was the average of three runs of 10−20 s each, then repeated at seven different scattering angles from 40° to 100°. We measured the diffusion coefficient D for at least three different concentrations for each sample, then used a linear fit (eq 6) to extrapolate data to $c = 0$ and extract a value for D_0. For samples where a simple cumulant analysis did not provide a good fit to the autocorrelation function (e.g., samples containing small size aggregates), diffusion coefficients and hydrodynamic radii were estimated by applying an inverse Laplace transform to $g^{(1)}(\tau,\theta)$

Properties of Hydrophilic Quantum Dots

J. Phys. Chem. B, Vol. 110, No. 41, 2006 **20311**
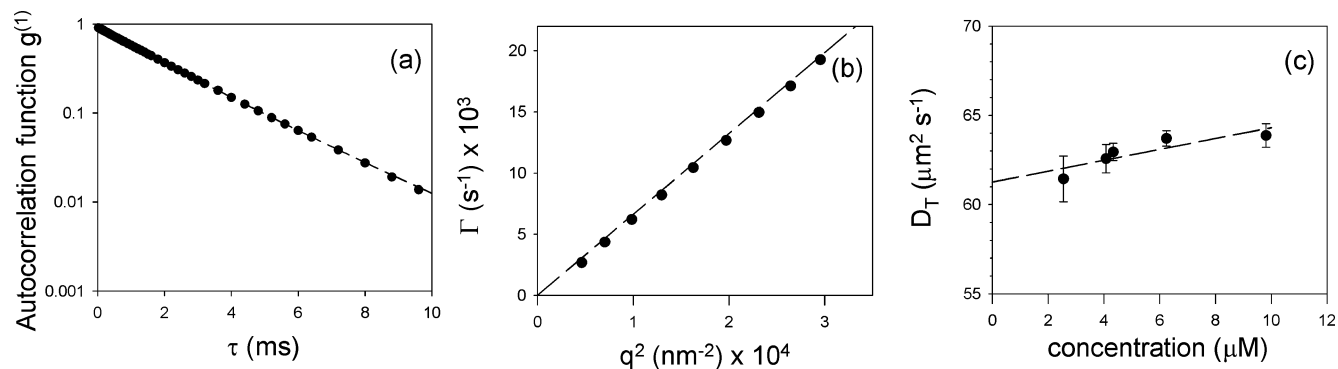
Figure 2. Examples showing plots of (a) the normalized autocorrelation function, $g^{(1)}(\tau)$ vs time, fitted with eq 4, (b) the decay rate Γ vs q^2, fitted with eq 3, and (c) the apparent diffusion coefficient vs QD concentration, fitted with eq 6.

(DTS software). This allowed determination of the proportion and average hydrodynamic sizes of aggregates and isolated nanoparticles.

Agarose Gel Electrophoresis. Gel electrophoresis is commonly used to separate proteins, oligonucleotides, or nanoparticles[33,34] based on their overall electrophoretic mobility, due to differences in molecular weight and/or overall charge. As the particle mobility under a static electric field depends on both particle size and charge, derivation of these two parameters requires more than a single measurement. Ferguson analysis uses concentration-dependent retardation of the particle by a gel pore network to estimate their average size.[35] This method was recently used to accurately measure the sizes of DNA-conjugated gold nanoparticles.[36] Within this analysis, the relationship between electrophoretic mobility M and gel concentration T is given by

$$\log_{10} M = \log_{10} M_0 - K_R T \qquad (10)$$

where M_0 is the particle mobility in absence of gel (i.e., in solution). The retardation coefficient, K_R, is strongly dependent on size due to the particle interactions with the gel network. For low-concentration gels, such as those made of one-dimensional fiber polymers such as agarose, $\sqrt{K_R}$ varies linearly with the particle size[35]

$$\sqrt{K_R} = AR_{\text{eff}} + B \qquad (11)$$

R_{eff} is the effective radius of the particle (close to the geometric radius), and A and B are constant parameters that depend on the gel network characteristics and experimental conditions (e.g., buffer and temperature).

To calibrate our gel mobility setup and determine A and B, we measured the mobility of gold nanocrystal standards of several nominal sizes ($R_{\text{eff}} = 2.4$, 4.8, 7.6, and 9.9 nm, from Ted Pella, Redding, CA) using different gel concentrations (low EEO agarose, Fisher Scientific, Suwanee, GA) in 10 mM Tris-borate with 2 mM EDTA (TBE) buffer (pH 9). These gold nanocrystals were overcoated with bis-(p-sulfonatophenyl)-phenylphosphine dihydrate (BSP) (Strem Chemicals, Newburyport, MA) to impart on them homogeneous negative surface charges.[36,37] QD samples were then run in parallel in the same gels as the gold particles. Samples were diluted to micromolar concentrations in a 3% glycerol TBE loading buffer immediately prior to use. An initial 30 V/cm electric field was applied for 20 s, followed by 15 V/cm for 15 min. QD bands were detected by fluorescence, while those of gold nanoparticles were detected by light absorption, using a Kodak 440 Digital Image Station (Rochester, NY).

For each sample, we measured the QD mobility in gels with 1, 1.5, 2, 2.5, and 3% agarose concentrations. For each gel concentration, three different gels were used to account for sample-to-sample variations. Using eq 10, we retrieved the retardation coefficient K_R for the measured sample, which was then used to determine R_{eff} for the nanocrystals using eq 11 with A and B obtained from the gold standards. In addition, extrapolation of the mobility to zero gel concentration allows derivation of the particle zeta potential.
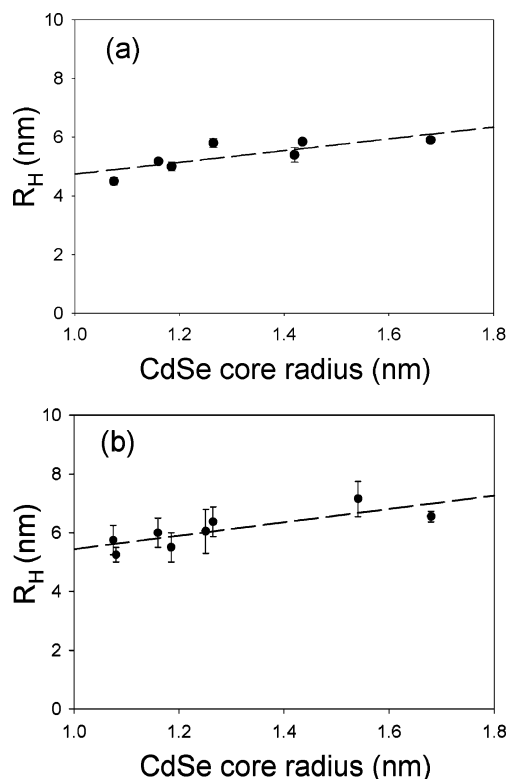
Zeta Potential and Electrophoretic Mobility Measurements. A charged particle in a buffer solution is surrounded by a counterion cloud, which can be separated into two distinct regions: a thin layer tightly packed around the surface (Stern layer) that migrates with the particle in the presence of an external electric field and a more diffuse layer that migrates in the opposite direction. The surface between these two regions is defined as the surface of shear, and its electric potential is referred to as the zeta potential, ζ. Closely related to the charge density at the particle surface, this potential controls colloidal properties such as stability and interparticle interactions. The solution electrophoretic mobility of the particle is related to ζ[38,39]

$$M_0 = \frac{2\epsilon\zeta}{3\eta_s} H(\kappa R) \qquad (12)$$

where ϵ is the solvent dielectric constant, κ is the Debye screening parameter, R is the particle geometric radius, and η_s is the solvent viscosity (e.g., $\eta_{\text{water}} \approx 0.89$ cP). The Henry function $H(\kappa R)$ varies between 1 and 1.5 as κR increases from 0 to ∞. In buffer solutions where the electrolyte concentration is high, the Debye screening parameter is large, and the Smoluchowski approximation $H = 1.5$ can be used.

The nanoparticle electrophoretic mobilities derived from the AGE (above) were compared to those extracted from LDV experiments. In the former, solution mobility was determined by fitting the gel mobility data derived from AGE to eq 10 and extrapolating to zero gel concentration. In the latter, the nanoparticle mobility is extracted from a measure of the inelastic frequency shift of the laser signal scattered by moving charged nanoparticles under applied electric field.[40] LDV measurements were performed using a ZetaSizer NanoSeries equipped with a He−Ne laser source ($\lambda = 633$ nm) and an avalanche photodiode for detection, controlled with DTS software. Micromolar concentration solutions of QDs were loaded into disposable folded capillary cells, and data were collected at 25 °C. Three runs of measurements were performed for each sample to determine sample-to-sample variations.
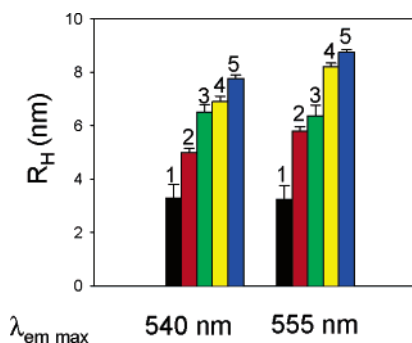
Figure 4. Comparison of the hydrodynamic radii for (1) CdSe TOP/TOPO-capped QDs in toluene, (2) CdSe−ZnS TOP/TOPO-capped QDs in toluene, (3) CdSe−ZnS DHLA-capped QDs in water, (4) CdSe−ZnS DHLA-PEG600-capped QDs in water, and (5) CdSe−ZnS DHLA-PEG1000-capped in water, for two QD series each having the same inorganic core, identified by the peak emission wavelength of the ZnS-overcoated QDs.

TABLE 2: Hydrodynamic Radii of Commercially Available Carboxylic-Acid-Modified QDs from Quantum Dot Corporation and Evident Technologies and Lipid-Encapsulated (DPPE-PEG2000) Hydrophilic QDs

sample	R_H (nm)	PDI
565-nm-COOH-QDC	7.1 ± 0.2	0.1
555-nm-QDs DPPE-PEG2000	10 ± 1.5	0.15
560-nm-T1-COOH Evident	30 ± 5	0.2
560-nm-T2-COOH Evident	14.7 ± 0.5	0.15

Figure 3. Hydrodynamic radii of CdSe−ZnS core−shell QDs capped with (a) TOP/TOPO in toluene and (b) DHLA in water, as a function of the CdSe geometric radius, R_{CdSe}. The fitted linear relations between R_H and R_{CdSe} are $R_H = 2R_{CdSe} + 2.7$ nm for TOP/TOPO-capped QDs, $R_H = 2.2R_{CdSe} + 3.2$ nm for DHLA-capped QDs. The intercept at the origin corresponds to what would be expected for ZnS core QDs with DHLA ligands.

Results and Discussion

Figure 2a shows a typical plot for $g^{(1)}(\tau)$ vs τ collected for the present QDs in either organic or buffer solutions along with the corresponding cumulant fit. For all solutions where aggregates were absent or negligible a second-order cumulant function provided a good fit to the data with low PDI values (PDI $\approx$ 0.05−0.2). Figure 2b shows a plot of the decay rate Γ vs q^2 along with a linear fit, a behavior consistent with dilute dispersions of scattering nanoparticles, as predicted above (eq 3). Data also indicate that the extracted diffusion coefficient and the hydrodynamic radius are independent of the scattering angle as expected for a regime where small scattering wave vectors are probed: $qR < 1$. Figure 2c shows a typical curve for the dependence of the effective diffusion coefficient D versus concentration for the same solutions. The observed linear increase further implies that the interparticle interactions in these QD media are repulsive and stabilizing, as indicated by the small positive slope of the linear fit to the data. In what follows, the hydrodynamic radius extracted for the various solutions used the extrapolated value for D at $c = 0$ and the Stokes−Einstein relationship (eq 7).

Effects of Core and Capping Ligands on the Hydrodynamic Size in Aggregate-Free Dispersions. We first examined the effects of varying the inorganic core size on the hydrodynamic radius for two sets of QDs; one is capped with the native TOP/TOPO and dispersed in toluene, while the other is capped with DHLA and dispersed in buffer (pH ∼9). All core−shell QDs have approximately five monolayers of ZnS overcoating. Figure 3 shows that there is a systematic increase in the measured R_H with increasing geometric core size R_{CdSe}, with a linear trend for both types of solutions. The hydrodynamic sizes

of the DHLA-capped QDs were about 10% larger than their TOP/TOPO-capped counterparts, which we attribute to a larger solvation layer around the QDs in buffer solutions due to the presence of carboxylic acid groups.

We next examined the influence of the nature and spatial extension of the capping ligands on the hydrodynamic radii of two batches/series of CdSe−ZnS nanocrystals (with two different emission maxima as synthesized in our laboratory). In each series, QDs were cap-exchanged with DHLA, DHLA-PEG600, and DHLA-PEG1000 and compared side-by-side with the native TOP/TOPO-capped CdSe and CdSe−ZnS nanocrystals. Results were further compared to the hydrodynamic radii measured for water-soluble QDs obtained with different solubilization strategies, namely, lipid-micelle-encapsulated nanocrystals and commercially available polymer-coated and carboxy-functionalized QDs (from Quantum Dot Corporation and Evident Technologies).[7,20] The commercial nanocrystals have emission peak locations close to those synthesized in our laboratory and should, in principle, have comparable core sizes. This assumption may be subject to a slight error, as schemes for QD preparation and surface functionalization are proprietary.

Figure 4 shows a systematic increase in R_H with the growth of a ZnS shell on the CdSe core for both sets of TOP/TOPO-capped QDs. Data also show that in buffer solutions substituting DHLA with the longer DHLA-PEG600 and DHLA-PEG1000 ligands resulted in a sizable increase in the measured R_H for both samples. The hydrodynamic sizes measured for the commercial QDs (shown in Table 2) vary substantially from one surface functionalization strategy to another, with polymer-encapsulated QDs (from Evident) being the largest. Further, variation in the polymer coating used can drastically change the measured R_H as shown for dispersions of T1 and T2 nanocrystals. Carboxy-capped nanocrystals provided by Quantum Dot Corporation and those encapsulated within lipid micelles are smaller in size (comparable to DHLA-capped nanocrystals). We should emphasize that the sizes measured for lipid-encapsulated QDs by DLS are in good agreement with

Properties of Hydrophilic Quantum Dots

J. Phys. Chem. B, Vol. 110, No. 41, 2006 **20313**

previously reported sizes measured by fluorescence correlation spectroscopy.[24]

Overall, the data shown in Figures 3 and 4 and Table 2 indicate that for all particles the measured hydrodynamic radii were consistently larger than the geometric sizes. They further indicate that these sizes are strongly (in some cases drastically) affected by the nature and lateral extension of the capping ligands or the coating layer used to achieve water compatibility. For example, for a ∼1.1 nm radius CdSe core (with first absorption peak at ∼477 nm), the five ZnS monolayers and the TOP/TOPO ligands represent an additional ∼1.2 and ∼1 nm, respectively. This would result in a CdSe−ZnS (core−shell) radius of 2.3 nm and a core−shell-plus-cap radius of ∼3.5 nm, significantly smaller than the measured hydrodynamic radius $R_H = 5$ nm. Similarly for 540-nm-emitting QDs ($R_{CdSe−ZnS} \approx$ 2.4 nm, with first absorption peak of CdSe only QDs at ∼505 nm) capped with DHLA-PEG, contributions from fully extended ligands (DHLA-PEG600 ≈ 2.5 nm and DHLA-PEG1000 ≈ 3.8 nm) result in geometric radii of ∼4.8 and ∼6.1 nm, respectively, which are still smaller than the R_H values measured in solution.

The data shown in Figures 3 and 4 indicate that R_H values measured for all other solutions were systematically larger than the geometric radii for the inorganic core or the core-plus-cap ($R_H/R_{CdSe−ZnS} > 1$). For example, the ratio $R_H/R_{CdSe−ZnS}$ extracted for the various capping strategies using DHLA-based ligands are ∼2.7 for DHLA, ∼2.9 for DHLA-PEG600, and ∼3 for DHLA-PEG1000 for 540-nm-emitting QDs. In comparison, the ratio for the other samples varied from ∼2.7 for the materials provided by Quantum Dot Corporation to ∼4 for lipid-encapsulated nanocrystals and exceeded 4 for the sets of QDs provided by Evident.

The larger values for the hydrodynamic radius measured for even the most compact ligand shell (e.g., TOP/TOPO and DHLA) is also consistent with what is expected for solid objects. It results from hydrodynamic contributions as evaluated by Oseen for hard spheres.[41] This is drastically different from what is predicted and measured for polymeric materials where the ratio between R_H and the radius of gyration is ∼$^2/_3$.[42] This major difference is due to the fact that solvent is able to penetrate within polymer coils diffusing in a solution but not hard spherical objects. However, the present nanoparticles are more complex than either solid spheres or macromolecules. They are made of solid CdSe−ZnS cores and are capped with ligands and coatings that behave more like polymers and can be penetrated by solvent molecules. The primary role of the surface functionalities (either simple cap molecules or larger polymeric chains) is to promote dispersion and stability of the nanocrystals in solutions. The measured R_H values for the various samples reflect this complexity. For instance, data show that contributions of the TOP/TOPO and DHLA capping shells to R_H are rather small due to their small spatial extension. In comparison, polymer coating employs large molecules to encapsulate the nanocrystals, and the result is a substantial increase in the overall hydrodynamic size of the resulting QDs. However, these ligands are not rigid, and their contributions cannot be treated as simple geometric increases to the radius. Overall, in treating the hydrodynamic aspects of the hydrophilic QDs, they can be viewed as a combination of solid impenetrable spherical cores and a more flexible polymer-like layer that strongly interacts with the surrounding solvent.

Reduced Solubility and Aggregation. While most solutions of QDs studied appeared to be aggregate-free, a very small number of aggregates were present in certain solutions of DHLA-capped and lipid-encapsulated QDs. This is reflected in
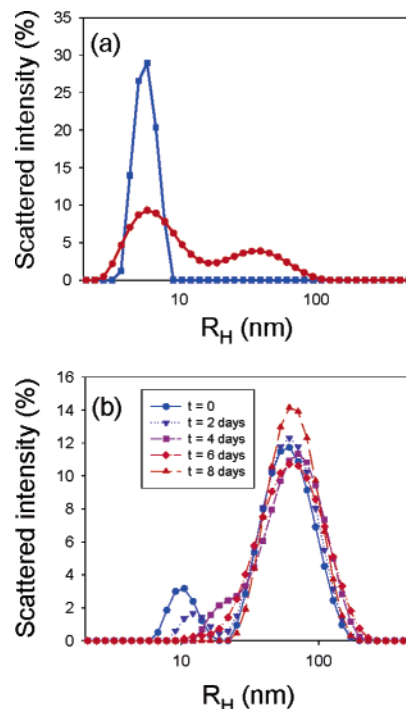
Figure 5. (a) Examples showing the size distribution of two DHLA QDs samples. One is made of a quasi-monodisperse population (squares), while the other one exhibits a small number (∼0.001%) of aggregates (circles). (b) Size distribution of MUA-capped QDs in water (pH 9) immediately after cap exchange and after 2, 4, 6, and 8 days.

plots of the Laplace inverse transform of the correlation function, which manifests as a second peak at a larger size (Figure 5a). However, these aggregates were always small and represented a ∼10^{-5} fraction of the overall nanoparticle population; their efficient detection was primarily due to the high sensitivity of DLS to the particle size (signal ∝ R^6). Furthermore, we found that even when aggregates were present in solutions of DHLA-capped QDs these samples were still stable and the percentage of such aggregates did not increase even after a few months (6−12 months) of storage at basic pH (data not shown). At pH < 7, larger-size aggregates progressively build up with time in solutions of DHLA-capped QDs in a few hours.

This represents a considerable improvement over capping CdSe−ZnS QDs with several monothiolated ligands, where QD aggregation in basic buffer solutions was recorded following transfer into water. Indeed, QDs cap-exchanged with MUA ligands following the same procedure as with DHLA and dispersed in water with potassium *tert*-butoxide (final pH ∼ 9) showed drastically different behavior that changed with storage time. The autocorrelation function could not be described using a simple cumulant analysis, where departure from the linear behavior was immediately observed. Laplace transform curves showed that a second peak (characteristic of aggregate presence in the solution) was detected immediately after cap exchange with MUA, along with a peak corresponding to the monomer population (Figure 5b). Moreover, this peak progressively dominated the data after a few days of storage, while the smaller size peak disappeared. This behavior clearly reflects a rather rapid aggregation buildup of MUA-capped QDs. In contrast, with DHLA-capped QDs even samples that exhibited a low degree of aggregation immediately after preparation were stable after several months of storage. This difference in dispersion stability between DHLA-capped and MUA-capped QDs may be attributed to the bidentate nature of the DHLA ligands, which

20314 *J. Phys. Chem. B, Vol. 110, No. 41, 2006*

Pons et al.
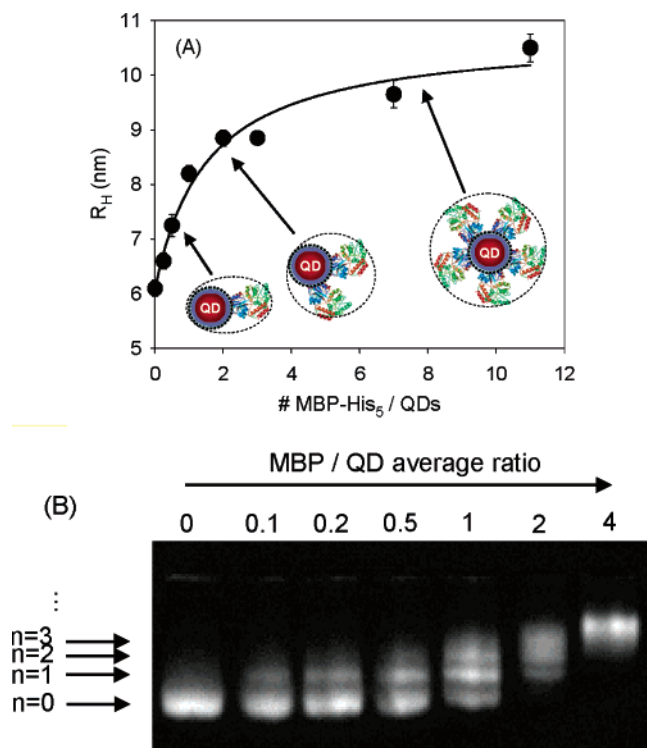
Figure 6. (A) Hydrodynamic radii of QD−MBP−His$_5$ bioconjugates as a function of the average number of proteins per QD. Schematics represent a CdSe−ZnS core−shell QD conjugated with 1 and 2 proteins and saturated with proteins. (B) Gel picture showing the separation of QD conjugates with different numbers of proteins per conjugate. At small ratios, samples show several mobility shift bands due to the Poisson distribution. These merge into a single band indicative of a homogeneous distribution of conjugate sizes as the average protein-to-QD ratio increases.

allow stronger ligand interactions (and binding) to the ZnS surface by two thiol groups instead of one offered by MUA ligands.

Hydrodynamic Sizes of Self-Assembled QD−Protein Conjugates. We monitored changes in the overall hydrodynamic sizes of QD−protein conjugates made by self-assembling increasing numbers of MBPs per nanocrystal. MBP was engineered to have a C-terminal polyhistidine tract that promotes self-assembly onto DHLA-capped CdSe−ZnS QDs (CdSe geometric core radius ∼1.6 nm by TEM) via metal-affinity interactions.[29,43] The data shown in Figure 6 indicate that R_H increased with increasing number of proteins per conjugate before saturating at a ratio exceeding 10 MBP−His$_5$ per QD. This number should not be confused with the actual maximum number of MBP−His$_5$ that can be conjugated to the QD surface. The latter is determined by steric considerations of how many proteins can be packed around a single nanocrystal. An inverse Laplace transform performed on the corresponding autocorrelation functions showed monomodal distributions, which indicates that there is no aggregate buildup during the self-assembly. This contrasts with what was reported for other bioconjugation methods, where significant particle aggregation has been observed.[44] We attribute the progressive increase in size to heterogeneity in the conjugate configuration, as the number of proteins self-assembled on a QD changed from one, two, three, etc. (as schematically depicted in Figure 6). MBP is an asymmetric protein ($M_w \cong 40\,600$) with an ellipsoid shape measuring $3 \times 4 \times 6.5$ nm^3.[45] We measured a hydrodynamic diameter of ∼6 nm for our MBP−His$_5$ in borate buffer solutions, a value close to what is expected for proteins with such

geometrical dimensions. The size measured near conjugate saturation is essentially the geometric superposition of the QD radius and MBP diameter. This implies that conjugates have a rather compact configuration, a result already confirmed using energy transfer experiments.[43,46] Our observation is different from those reported in another study of QD−protein conjugation using DLS, where the size of the QDs increased when conjugated to one protein but did not further increase with the conjugation of subsequent proteins.[47]

This significant size increase upon conjugation to proteins and the anticipated heterogeneity of the conjugates with small protein-to-QD ratios can be compared to information extracted from gel electrophoresis measurements, where discrete bands corresponding to conjugates with exact valency (e.g., a protein-to-QD ratio of 1) were isolated based on heterogeneity in size, similar to what has been observed with other gold or semiconductor nanoparticle conjugates (Figure 6b).[48,49] Heterogeneity in the number of proteins per QD is particularly clear for lower average proteins-to-QD ratios and follows qualitatively a Poisson distribution expected from a self-assembly process. For example, for 1 protein per QD on average, the expected QD population distribution is ∼$1/3$ with no proteins, ∼$1/3$ with one protein, and ∼$1/3$ with more than one protein per QD. The gel separation measurements somewhat mimic our DLS observations and provide additional insight into the population distribution of our self-assembled QD conjugates. Knowledge of this distribution is a crucial point in the characterization of self-assembled QD-based biosensors, especially when using QDs as energy transfer donors. Furthermore, this may provide a very simple tool for isolating a 1:1 QD−protein conjugate, an important requirement to avoid cross-linking of the particle with several targets in cellular imaging or biosensing applications.

QD Geometric Sizes and Zeta Potentials. The gel picture in Figure 7 shows that, similar to gold standards, there is single band in the mobility shift for QD samples, indicating that during migration nanocrystals and their conjugates remain homogeneously dispersed in single populations, with homogeneous zeta potentials. Figure 7 also shows that the mobility plots for the QD samples follow the same trends as the gold standards when the QD size is varied. Table 3 summarizes size and zeta potential results from Ferguson analysis of mobility data obtained for several sizes of DHLA-capped QDs, commercially available carboxylic-acid-functionalized QDs, and DHLA-QDs conjugated with an average of 20 MBP−His$_5$.

While some DHLA-capped QDs samples exhibited a signal contribution from aggregates to the autocorrelation function in DLS, AGE experiments did not reveal the presence of any aggregates, which would form separate bands in the gels (Figure 7). This is due to the fact that AGE is much less sensitive to aggregates than DLS, because it relies on fluorescence or absorbance detection (aggregate signal ∝ N), instead of light scattering (aggregate signal ∝ $R^6 \propto N^2$), where N is the number of QDs per aggregate. This confirms that the small aggregates observed by DLS in a few DHLA-capped QD samples represent indeed negligible population fractions.

Overall the measured R_{eff} are subject to slightly larger errors (10−20%) than DLS above. Regardless, R_{eff} values for DHLA-capped QDs are smaller than R_H and are closer to the geometric sizes as measured by atomic force microscopy;[46] they increase slightly with the size of the inorganic core. R_{eff} of QD−MBP−His$_5$ conjugates is close to the hydrodynamic radius measured by DLS and is consistent with the geometric sizes of the QD and protein. For this high average protein-to-QD ratio, the conjugates are expected to exhibit similar radii throughout the

Properties of Hydrophilic Quantum Dots

J. Phys. Chem. B, Vol. 110, No. 41, 2006 **20315**
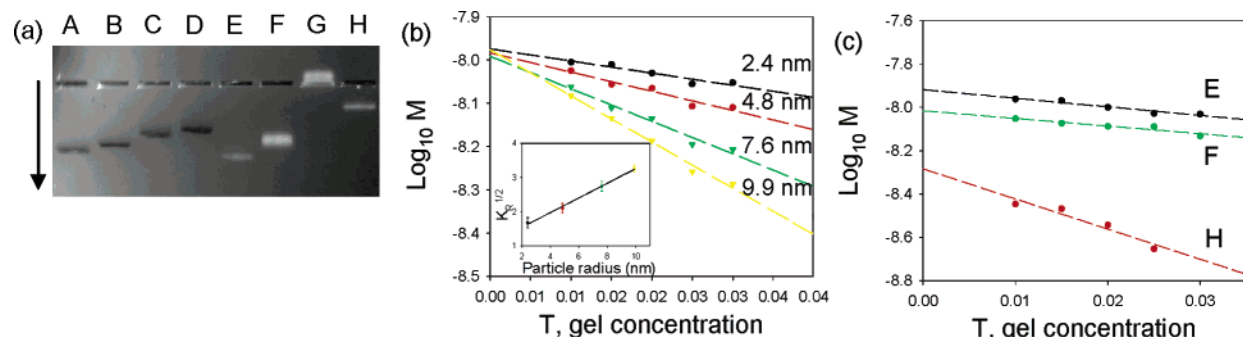
Figure 7. (a) Agarose gel picture showing BSP-coated 2.4, 4.8, 7.6, and 9.9 nm radius gold nanoparticles (A–D) visualized by absorption, and 540 nm QDs capped with DHLA (E), a 1:1 mixture of DHLA/DHLA-PEG600 (F), DHLA-PEG600 (G), and QD–20MBP–His$_5$ conjugates (H). QD bands were visualized by fluorescence. (b) Electrophoretic mobility of gold particle standards as a function of gel concentration. For each size, the corresponding retardation coefficient, K_R, is the slope of the linear fit. The inset shows $K_R^{1/2}$ as a function of the particle radius for the gold particles. (c) Electrophoretic mobility of QD samples vs gel concentration.
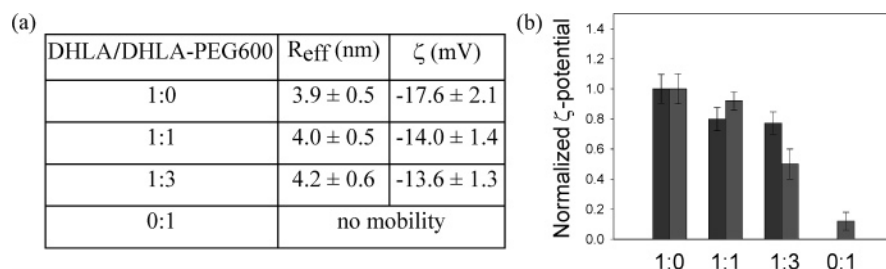
Figure 8. (a) Radii and zeta potentials of 540-nm-QDs capped with a mixture of DHLA and DHLA-PEG600 ligands obtained by AGE, using different ratios of DHLA/DHLA-PEG600 during cap exchange. (b) Comparison of results obtained by Ferguson analysis (dark gray) and LDV (light gray). Zeta potentials have been normalized with respect to the sample made of DHLA-capped QDs (ζ(1:0) = −17.6 mV by AGE; ζ(1:0) = −25 mV by LDV) for easier comparison.

TABLE 3: Effective Radii and Zeta Potentials Obtained by Ferguson Analysis (AGE) and DLV for Different DHLA- and DHLA-PEG600-Capped QDs, Carboxylic-Acid-Modified QDs from Quantum Dot Corporation, and DHLA-Capped QDs Conjugated with an Average of 20 MBP−His$_5$ per QD

sample	R_{eff} (nm)	ζ (mV) (AGE)	ζ (mV) (LDV)
510-nm-DHLA QDs	3.2 ± 0.7	−23.1 ± 2.2	−26 ± 3
540-nm-DHLA QDs	3.9 ± 0.5	−17.6 ± 1.7	−25 ± 3
555-nm-DHLA QDs	3.5 ± 0.6	−24.2 ± 2.3	
590-nm-DHLA QDs	4.4 ± 0.5	−25.3 ± 2.4	−27 ± 4
540-nm-QD-DHLA-PEG600	no mobility		−2.5 ± 1.5
565-nm-COOH-Qdot	7.1 ± 0.3	−27.1 ± 2.6	
540-nm-QD/20MBPs	11.5 ± 1	−7.6 ± 0.7	

Poisson distribution and give rise to a homogeneous mobility. The effective radii of the QDs from Quantum Dot Corporation were significantly larger than those of DHLA-capped QDs, due to the thickness of the polymer coating. We note that the correlation between the size derived from AGE (approximately the geometric size) and the size derived from DLS (hydrodynamic size) depends on the type of particle coating. For example, carboxy-polymer-coated QDs exhibit similar geometric and hydrodynamic sizes, while DHLA-capped QD geometric sizes are significantly smaller than their hydrodynamic sizes. This behavior may be attributed to the contribution of a larger polymer-encapsulating layer on the commercial QDs, which would hinder the QD migration and reduce its overall mobility in the gel compared to the DHLA capping. The geometrically larger polymer-coated QDs may be less able to access tightly confined spaces (pores) in the gel. These data provide an illustration of the complementarity of AGE and DLS measurements.

The zeta potential of DHLA-capped QDs extracted from AGE measurements are in reasonable agreement with those measured by LDV (Table 3). They confirm the presence of negative charges on the surfaces of the QDs, due to the carboxylic end groups on the ligands. Conversely, when DHLA was substituted with DHLA-PEG600 the electrophoretic mobilities measured with LDV and AGE were very small and negligible, respectively. The rather uniform zeta potentials of DHLA-capped QDs reflect similar charge surface densities. The zeta potential of 565-nm-COOH-Qdot was similar to that measured for DHLA-capped QDs. In contrast, carboxylic-acid-modified T2 QDs from Evident Technologies were completely immobile in the gels at pH 9, revealing the absence of net charge under these conditions. This might be due to detachment of the charged lipid from the surface of the QDs under electric field.

Finally, we investigated the properties of QDs capped with a mixture of different ligands. Mixed surface coating offers a promising method for providing multiple functionalities to nanoparticles. Measurement of the size and zeta potential of the particles gives an insight into the composition of the mixed surface and its properties. Here, we examined QDs capped with mixed surfaces composed of DHLA and DHLA-PEG600 (Figure 8a). The size of the particle slightly increases while the zeta potential decreases with a decreasing DHLA-to-DHLA-PEG600 ratio in the solution used for cap exchange. This reflects the progressive substitution of DHLA with DHLA-PEG ligands during cap exchange and transfer into buffer. Bands in the gel remain narrow, which indicates that the composition of the mixed surfaces is relatively homogeneous throughout the QD sample. These results were confirmed by LDV (Figure 8b).

Conclusion

Control over the QD size and charge is a key element in the design of compact, well-dispersed QDs with limited nonspecific interactions in biological environments. We have demonstrated that DLS, AGE, and LDV are powerful and complementary

20316 *J. Phys. Chem. B, Vol. 110, No. 41, 2006*

Pons et al.

tools to characterize sizes and charges of hydrophilic QDs. We examined and compared hydrodynamic radii and zeta potentials of a series of CdSe−ZnS QDs made hydrophilic using different solubilization strategies. We have shown that the nanoparticle hydrodynamic size strongly depends on the core radius as well as size and type of capping ligands or coating materials. Hydrophilic QDs obtained by cap exchange with small bidentate ligands are generally smaller than polymer-coated or lipid-encapsulated QDs. Our set of data further showed that CdSe−ZnS QDs capped with dithiol-terminated ligands are more stable and less prone to aggregation than those functionalized with monothiol-terminated ligands. We also observed that the QD zeta potential is homogeneous in each sample and is correlated with the surface composition. Finally, our results indicate that these techniques can be used to monitor the conjugation of QDs with biomolecules and characterize the formed conjugate sizes and dispersions.

References and Notes

(1) Bruchez, M.; Moronne, M.; Gin, P.; Weiss, S.; Alivisatos, A. P. *Science* **1998**, *281*, 2013−2016.

(2) Chan, W. C. W.; Nie, S. M. *Science* **1998**, *281*, 2016−2018.

(3) Mattoussi, H.; Mauro, J. M.; Goldman, E. R.; Anderson, G. P.; Sundar, V. C.; Mikulec, F. V.; Bawendi, M. G. *J. Am. Chem. Soc.* **2000**, *122*, 12142−12150.

(4) Alivisatos, P. *Nat. Biotechnol.* **2004**, *22*, 47−52.

(5) Michalet, X.; Pinaud, F. F.; Bentolila, L. A.; Tsay, J. M.; Doose, S.; Li, J. J.; Sundaresan, G.; Wu, A. M.; Gambhir, S. S.; Weiss, S. *Science* **2005**, *307*, 538−544.

(6) Medintz, I. L.; Uyeda, H. T.; Goldman, E. R.; Mattoussi, H. *Nat. Mater.* **2005**, *4*, 435−446.

(7) Dubertret, B.; Skourides, P.; Norris, D. J.; Noireaux, V.; Brivanlou, A. H.; Libchaber, A. *Science* **2002**, *298*, 1759−1762.

(8) Jaiswal, J. K.; Mattoussi, H.; Mauro, J. M.; Simon, S. M. *Nat. Biotechnol.* **2003**, *21*, 47−51.

(9) Dahan, M.; Levi, S.; Luccardini, C.; Rostaing, P.; Riveau, B.; Triller, A. *Science* **2003**, *302*, 442−445.

(10) Kim, S.; Lim, Y. T.; Soltesz, E. G.; De Grand, A. M.; Lee, J.; Nakayama, A.; Parker, J. A.; Mihaljevic, T.; Laurence, R. G.; Dor, D. M.; Cohn, L. H.; Bawendi, M. G.; Frangioni, J. V. *Nat. Biotechnol.* **2004**, *22*, 93−97.

(11) Goldman, E. R.; Anderson, G. P.; Tran, P. T.; Mattoussi, H.; Charles, P. T.; Mauro, J. M. *Anal. Chem.* **2002**, *74*, 841−847.

(12) Goldman, E. R.; Clapp, A. R.; Anderson, G. P.; Uyeda, H. T.; Mauro, J. M.; Medintz, I. L.; Mattoussi, H. *Anal. Chem.* **2004**, *76*, 684−688.

(13) Gao, X. H.; Cui, Y. Y.; Levenson, R. M.; Chung, L. W. K.; Nie, S. M. *Nat. Biotechnol.* **2004**, *22*, 969−976.

(14) Lidke, D. S.; Nagy, P.; Heintzmann, R.; Arndt-Jovin, D. J.; Post, J. N.; Grecco, H. E.; Jares-Erijman, E. A.; Jovin, T. M. *Nat. Biotechnol.* **2004**, *22*, 198−203.

(15) Murray, C. B.; Norris, D. J.; Bawendi, M. G. *J. Am. Chem. Soc.* **1993**, *115*, 8706−8715.

(16) Qu, L. H.; Peng, Z. A.; Peng, X. G. *Nano Lett.* **2001**, *1*, 333−337.

(17) Hines, M. A.; Guyot-Sionnest, P. *J. Phys. Chem.* **1996**, *100*, 468−471.

(18) Dabbousi, B. O.; Rodriguez-Viejo, J.; Mikulec, F. V.; Heine, J. R.; Mattoussi, H.; Ober, R.; Jensen, K. F.; Bawendi, M. G. *J. Phys. Chem. B* **1997**, *101*, 9463−9475.

(19) Uyeda, H. T.; Medintz, I. L.; Jaiswal, J. K.; Simon, S. M.; Mattoussi, H. *J. Am. Chem. Soc.* **2005**, *127*, 3870−3878.

(20) Wu, X. Y.; Liu, H. J.; Liu, J. Q.; Haley, K. N.; Treadway, J. A.; Larson, J. P.; Ge, N. F.; Peale, F.; Bruchez, M. P. *Nat. Biotechnol.* **2003**, *21*, 41−46.

(21) Pellegrino, T.; Manna, L.; Kudera, S.; Liedl, T.; Koktysh, D.; Rogach, A. L.; Keller, S.; Radler, J.; Natile, G.; Parak, W. J. *Nano Lett.* **2004**, *4*, 703−707.

(22) Mattoussi, H.; Cumming, A. W.; Murray, C. B.; Bawendi, M. G.; Ober, R. *Phys. Rev. B* **1998**, *58*, 7850−7863.

(23) Liedl, T.; Keller, S.; Simmel, F. C.; Radler, J. O.; Parak, W. J. *Small* **2005**, *1*, 997−1003.

(24) Doose, S.; Tsay, J. M.; Pinaud, F.; Weiss, S. *Anal. Chem.* **2005**, *77*, 2235−2242.

(25) Nirmal, M.; Dabbousi, B. O.; Bawendi, M. G.; Macklin, J. J.; Trautman, J. K.; Harris, T. D.; Brus, L. E. *Nature* **1996**, *383*, 802−804.

(26) Peng, Z. A.; Peng, X. G. *J. Am. Chem. Soc.* **2001**, *123*, 183−184.

(27) Yu, W. W.; Qu, L. H.; Guo, W. Z.; Peng, X. G. *Chem. Mater.* **2003**, *15*, 2854−2860.

(28) Medintz, I. L.; Goldman, E. R.; Lassman, M. E.; Mauro, J. M. *Bioconjugate Chem.* **2003**, *14*, 909−918.

(29) Medintz, I. L.; Clapp, A. R.; Mattoussi, H.; Goldman, E. R.; Fisher, B.; Mauro, J. M. *Nat. Mater.* **2003**, *2*, 630−638.

(30) Brown, W. *Dynamic Light Scattering: The Method and Some Applications*; Clarendon Press: Oxford, 1993.

(31) Berne, B. J.; Pecora, R. *Dynamic Light Scattering: With Applications to Chemistry, Biology, and Physics*; Dover Publishing: Mineola, NY, 2000.

(32) Koppel, D. E. *J. Chem. Phys.* **1972**, *57*, 4814−4820.

(33) Parak, W. J.; Gerion, D.; Zanchet, D.; Woerz, A. S.; Pellegrino, T.; Micheel, C.; Williams, S. C.; Seitz, M.; Bruehl, R. E.; Bryant, Z.; Bustamante, C.; Bertozzi, C. R.; Alivisatos, A. P. *Chem. Mater.* **2002**, *14*, 2113−2119.

(34) Gerion, D.; Pinaud, F.; Williams, S. C.; Parak, W. J.; Zanchet, D.; Weiss, S.; Alivisatos, A. P. *J. Phys. Chem. B* **2001**, *105*, 8861−8871.

(35) Rodbard, D.; Chrambach, A. *Proc. Natl. Acad. Sci. U.S.A.* **1970**, *65*, 970−977.

(36) Park, S.; Brown, K. A.; Hamad-Schifferli, K. *Nano Lett.* **2004**, *4*, 1925−1929.

(37) Loweth, C. J.; Caldwell, W. B.; Peng, X. G.; Alivisatos, A. P.; Schultz, P. G. *Angew. Chem., Int. Ed.* **1999**, *38*, 1808−1812.

(38) Henry, D. C. *Proc. R. Soc. London, Ser. A* **1931**, *133*, 106−129.

(39) Schmitz, K. *An Introduction to Dynamic Light Scattering by Macromolecules*; Academic Press: San Diego, CA, 1990.

(40) Ware, B. R.; Flygare, W. H. *Chem. Phys. Lett.* **1971**, *12*, 81−85.

(41) Landau, L. D.; Lifschitz, E. M. *Fluid Mechanics*; Pergamon Press: Oxford, U. K., 1993.

(42) Benoit, H.; Doty, P. *J. Phys. Chem.* **1953**, *57*, 958−963.

(43) Clapp, A. R.; Medintz, I. L.; Mauro, J. M.; Fisher, B. R.; Bawendi, M. G.; Mattoussi, H. *J. Am. Chem. Soc.* **2004**, *126*, 301−310.

(44) Nehilla, B. J.; Vu, T. Q.; Desai, T. A. *J. Phys. Chem. B* **2005**, *109*, 20724−20730.

(45) Spurlino, J. C.; Lu, G.-Y.; Quiocho, F. A. *J. Biol. Chem.* **1991**, *266*, 5202−5219.

(46) Medintz, I. L.; Konnert, J. H.; Clapp, A. R.; Stanish, I.; Twigg, M. E.; Mattoussi, H.; Mauro, J. M.; Deschamps, J. R. *Proc. Natl. Acad. Sci. U.S.A.* **2004**, *101*, 9612−9617.

(47) Ipe, B. I.; Shulka, A.; Lu, H.; Zou, B.; Rehage, H.; Niemeyer, C. M. *ChemPhysChem* **2006**, *7*, 1112−1118.

(48) Sperling, R. A.; Pellegrino, T.; Li, J. K.; Chang, W. H.; Parak, W. J. *Adv. Funct. Mater.* **2006**, *16*, 943−948.

(49) Fu, A. H.; Micheel, C. M.; Cha, J.; Chang, H.; Yang, H.; Alivisatos, A. P. *J. Am. Chem. Soc.* **2004**, *126*, 10832−10833.